

DUST CONTINUUM AND POLARIZATION FROM ENVELOPE TO CORES IN STAR FORMATION: A CASE STUDY IN THE W51 NORTH REGION

YA-WEN TANG^{1,2,3}, PAUL T. P. HO^{3,4}, PATRICK M. KOCH³, STEPHANE GUILLOTEAU^{1,2}, AND ANNE DUTREY^{1,2}

Draft version July 3, 2018

ABSTRACT

We present the first high-angular resolution (up to $0''.7$, ~ 5000 AU) polarization and thermal dust continuum images toward the massive star-forming region W51 North. The observations were carried out with the Submillimeter Array (SMA) in both the subcompact (SMA-SubC) and extended (SMA-Ext) configurations at a wavelength of $870 \mu\text{m}$. W51 North is resolved into four cores (SMA1 to SMA4) in the $870 \mu\text{m}$ continuum image. The associated dust polarization exhibits more complex structures than seen at lower angular resolution. We analyze the inferred morphologies of the plane-of-sky magnetic field (B_{\perp}) in the SMA1 to SMA4 cores and in the envelope using the SMA-Ext and SMA-SubC data. These results are compared with the B_{\perp} archive images obtained from the CSO and JCMT. The polarization percentage is about 1 % to 4 %, and it is found to decrease with higher intensity in our SMA images, which is a similar trend as previously reported in the CSO and JCMT data. A correlation between dust intensity gradient position angles ($\phi_{\nabla I}$) and magnetic field position angles (ϕ_B) is found in the CSO, JCMT and both SMA data sets. This correlation is further analyzed quantitatively. A systematically tighter correlation between $\phi_{\nabla I}$ and ϕ_B is found in the cores, whereas the correlation decreases in outside-core regions. Magnetic field-to-gravity force ratio (Σ_B) maps are derived using the newly developed polarization - intensity gradient method by Koch et al. (2012a). We find that the force ratios tend to be small ($\Sigma_B \lesssim 0.5$) in the cores in all 4 data sets. In regions outside of the cores, the ratios increase or the field is even dominating gravity ($\Sigma_B > 1$). This possibly provides a physical explanation of the tightening correlation between $\phi_{\nabla I}$ and ϕ_B in the cores: the more the B field lines are dragged and aligned by gravity, the tighter the correlation is. Finally, we propose a schematic scenario for the magnetic field in W51 North to interpret the four polarization observations at different physical scales.

Subject headings: ISM: individual (W51 d) – individual (W51 North) – individual (W51 IRS2) – individual (W51 A) – ISM: magnetic fields – polarization – stars: formation

1. INTRODUCTION

Stars form in giant molecular clouds under the threads of turbulence (see review by Mac Low & Klessen 2004) and large-scale magnetic (B) fields (e.g. Crutcher 1999). Theoretically, the significance of the B field influences how structures are formed, such as the density contrast within structures (Kowal et al. 2007), the star formation rate (Vázquez-Semadeni et al. 2005; Price & Bate 2008) and the suppressed fragmentation (Price & Bate 2007; Hennebelle et al. 2011). However, the B fields in star-forming clouds are not well constrained observationally, because they are difficult to detect. The Zeeman effect on spectral lines can trace the B field strength along the line of sight (e.g. Fish & Reid 2006; Vlemmings et al. 2006; Falgarone et al. 2008; Surcis et al. 2012). The B field properties on the plane of sky, B_{\perp} , rely on polarization studies.

Dust grains are thought to be partly aligned with their minor axes to the magnetic field lines. Several

alignment mechanisms have been studied (see review by Lazarian 2000), and radiative torques are likely to be responsible for the dust alignment (Draine & Weingartner 1996, 1997; Cho & Lazarian 2005; Lazarian & Hoang 2007). Due to the difference in emissivity along the major and minor axes of the elongated dust grains, the thermal emission from dust grains can therefore be partly linearly polarized perpendicular to the field lines (Hildebrand 1988). The B_{\perp} morphology can therefore be inferred by rotating the detected polarization of the thermal emission by 90° . Linear polarization of thermal dust emission has been imaged at far infrared and at submillimeter (submm) in several star-forming clouds (e.g., Greaves et al. 1994; Chrysostomou et al. 2002; Vaillancourt et al. 2008; Dotson et al. 2010; Matthews et al. 2009). To further resolve the star-forming cores, higher angular resolution observations of the millimeter (mm) and submm continuum emission are powerful, because the continuum is mostly optically thin at these wavelengths. Both massive and low mass star-forming cores have been imaged in linear polarization with an angular resolution of a few arcsecond in the mm and submm regime (e.g., Lai et al. 2001; Girart et al. 2006; Tang et al. 2009a,b; Rao et al. 2009; Tang et al. 2010). W51 North is another good candidate to study the massive star formation processes. It has strong dust emission at mm wavelengths. This increases the possibilities to detect polarization, because

Electronic address: ywtang@asiaa.sinica.edu.tw

¹ Université de Bordeaux, Observatoire Aquitain des Sciences de l'Univers, 2 rue de l'Observatoire, BP 89, F-33271 Floirac Cedex, France

² CNRS, UMR 5804, Laboratoire d'Astrophysique de Bordeaux, 2 rue de l'Observatoire, BP 89, F-33271 Floirac Cedex, France

³ Academia Sinica, Institute of Astronomy and Astrophysics, Taipei, Taiwan

⁴ Center for Astrophysics, 60 Garden Street, Cambridge, MA 02138

the linear polarization percentage is typically only a few percent in star-forming regions and therefore, difficult to measure.

The W51 North region is active in star formation. It lies within the HII region complex G49.5-0.4 in W51 A, west of the W51 giant molecular cloud. It is located 5–8 kpc away in the Sagittarius spiral arm (Genzel et al. 1981; Imai et al. 2002; Xu et al. 2009). In this paper, we adopt a distance of 7 kpc. At radio wavelengths (1.3 cm and 3.6 cm), an edge-brightened cometary HII region, W51 d, and an ultracompact HII (UCHII) region, W51 d2, (Gaume et al. 1993) were detected. The brightest mm source is 2'' to the east of W51 d2 (Zhang et al. 1998; Sollins et al. 2004; Zapata et al. 2008). Associated with this mm source, a group of H₂O, OH and SiO masers were detected, and it has been also named as "the dominant center" (Schneps et al. 1981). In this dominant center, infall signatures have been detected (Sollins et al. 2004; Zapata et al. 2008, 2009). The outflows from the dominant center were reported to have position angles between 105° and 150° (Eisner et al. 2002; Zhang et al. 1998; Zapata et al. 2009). An embedded protostar candidate OKYM 1 (also called KJD 3, Kraemer et al. 2001), 1'' to the north-east of the dominant center, was reported (Okamoto et al. 2001; Barbosa et al. 2008). This region is, thus, a very active star-forming complex where several regions are in different evolutionary stages.

Linear polarization of thermal dust continuum toward W51N was detected in the submm regime with single dish telescopes. At wavelengths of 350 μ m with an angular resolution of 20'', Dotson et al. (2010) show that the polarization is mainly uniform across W51 North. In contrast, at 850 μ m, both Chrysostomou et al. (2002) and Matthews et al. (2009) show that there are more variations in the polarization orientations. Since there is probably multiple ongoing star formation in W51 North, higher angular resolution measurements of the polarization are important to reveal the physical conditions at this scale. Hereafter, the data obtained from Dotson et al. (2010) and Chrysostomou et al. (2002) are called CSO and JCMT, respectively.

Here, we report the new Submillimeter Array (SMA) 870 μ m continuum images and the detection of linearly polarized emission of dust continuum at an angular resolution up to 0''.7 toward the W51 North. Polarization percentages and position angles, and the correlation between position angle and intensity are studied. With the goal of providing a more complete scenario of the role of the magnetic field over several scales, we further compare our new polarization results at a scale of 60 mpc with the published polarization images at a scale of a few pc at the submm regime from CSO and JCMT. The observations and data reduction are described in section 2. The observational results are shown in section 3. In section 4, we will present the detailed quantitative analyses of the polarization of our new observational results, and we will provide a physical explanation of the derived values. We then propose a schematic scenario for the magnetic field in W51 North. We draw conclusions and summarize in section 5.

2. OBSERVATIONS AND DATA REDUCTION

TABLE 1
OBSERVATIONAL PARAMETERS

Parameter	SMA-Ext	SMA-SubC
Date	2008 Jul 13	2009 Sep 11
Available Antennae	7	6
Gain Calibrator	1751+096, 1925+211	1751+096
Flux Calibrator	Titan	Uranus
Bandpass/Pol Calib.	3c454.3	3c454.3
Baseline range ($k\lambda$)	30 to 262	10 to 30
σ_I (Jy beam ⁻¹)	0.06	0.19
σ_{I_p} (mJy beam ⁻¹)	3	15
θ_{syn}	0''.7×0''.6	4''.1×3''.6
P.A. of θ_{syn}	-57°	20°

NOTE. — σ_I and σ_{I_p} are the noise levels of Stokes I and the polarized intensity (I_p), respectively.

The observations were carried out using the SMA (Ho et al. 2004)⁵ in the extended and subcompact configuration, respectively. In the following, the results obtained from the extended and the subcompact configuration are called SMA-Ext and SMA-SubC, respectively. The synthesized beams (angular resolutions), θ_{syn} , of SMA-Ext and SMA-SubC are $\sim 0''.7$ and $4''$, respectively. In both observations, the local oscillator frequency was tuned to 341.482 GHz (870 μ m). The observational details are listed in Table 1.

The SMA-Ext observation was carried out along with W51 e2/e8. These two sources shared the same calibrators and were reduced and imaged in the same way. The details of the observation and data reduction are described in Tang et al. (2009). In brief, the SMA-Ext data were reduced and imaged in MIRIAD following standard procedures. An additional calibration on the instrumental polarization (also called the leakage terms) was derived using the calibrator 3c454.3. The largest size scale which could be sampled in the extended track was $\sim 8''$ (0.3 pc). For the subcompact track, the data were reduced with MIR and then imaged using MIRIAD.

The position angle of the polarization, ϕ_{pol} , is calculated from: $\phi_{\text{pol}} = \frac{1}{2} \tan^{-1} \frac{U}{Q}$, increasing counter-clockwise in the range -90° to 90° . The strength, I_p , and percentage, $P(\%)$, of the linearly polarized emission are calculated from: $I_p^2 = Q^2 + U^2 - \sigma_{Q,U}^2$ and $P(\%) = I_p/I$, respectively. Here, $\sigma_{Q,U}$ is the noise level of the Stokes Q and U images, and it is also the bias correction due to the positive measure of I_p (Leahy 1989; Wardle & Kronberg 1974).

The primary beam (field of view) of the SMA at 345 GHz is $\sim 30''$. All of the presented SMA maps in the following have been corrected for the primary beam attenuation. The presented maps were constructed with natural weighting. The phase center is at Right Ascension (J2000)=19^h23^m40.05^s, Declination (J2000)=14°31'5''.0.

3. RESULTS

3.1. Continuum Emission

3.1.1. Dense Structures: SMA 1 to SMA4

⁵ The Submillimeter Array is a joint project between the Smithsonian Astrophysical Observatory and the Academia Sinica Institute of Astronomy and Astrophysics and is funded by the Smithsonian Institution and the Academia Sinica.

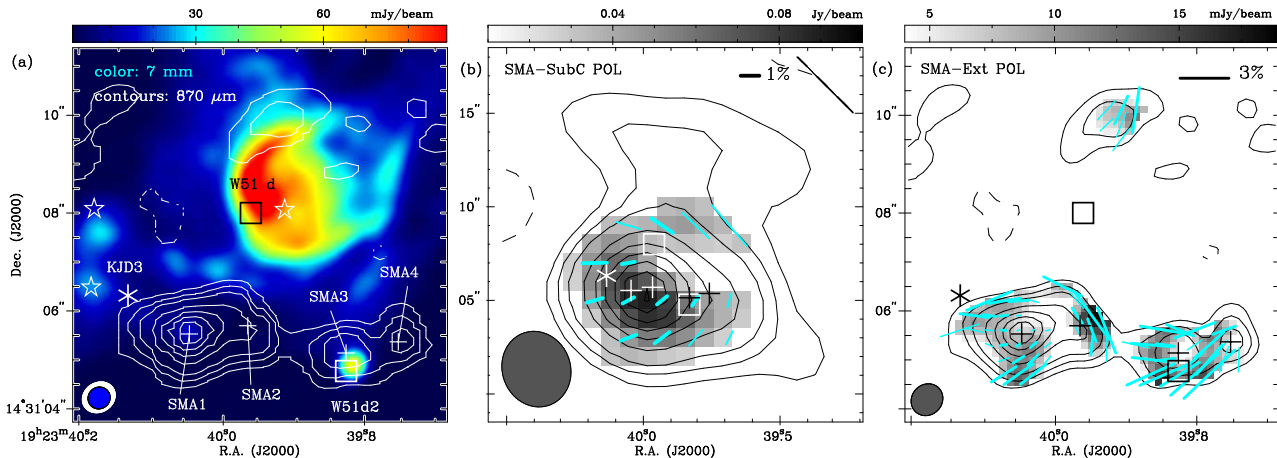


FIG. 1.— (a): Continuum map at $870\ \mu\text{m}$ obtained from SMA-Ext and continuum map at $7\ \text{mm}$ from EVLA (image adopted from Zapata et al. 2008) shown in white contours and color scale, respectively. The small squares mark the position of the edge-brightened cometary/shell-like HII region W51 d and W51 d2 (Gaume et al. 1993). The infrared source KJD3 (also called OKMY 1) is marked as *. The stars mark the identified O stars by Okamoto et al. (2001). The pluses mark the resolved submillimeter sources SMA 1 to 4. (b) and (c): Polarization (segments) and polarized intensity (grey scale) from the subcompact track (panel b) and extended track (panel c). The lengths of the polarization segments are proportional to the polarization percentages. The plotted thick and thin segments are above 3 and between 2 to $3\ \sigma_{1p}$, respectively. The synthesized beams are shown as ellipses in the lower-left corners. Contours are at -3 (dash) and $3, 6, 10, 20, 30, 40, \dots \times 0.06$ and $0.19\ \text{Jy beam}^{-1}$ for SMA-Ext and SMA-SubC, respectively.

TABLE 2
DUST COMPONENTS

Name	R.A.	Dec.	Flux (Jy)	Deconvolved Size ($'' \times ''$), PA($^\circ$)	$\langle\phi_{\text{pol}}\rangle$	$\sigma_{\phi_{\text{pol}}}$	Note
SMA1	19:23:40.047	14:31:5.53	8.69 ± 0.27	$(0.98 \pm 0.03) \times (0.68 \pm 0.02)$, -89 ± 3	-25	51	dominant center
SMA2	19:23:39.970	14:31:5.70	2.59 ± 0.24	$(1.12 \pm 0.07) \times (0.28 \pm 0.11)$, 39 ± 3	4	30	-
SMA3	19:23:39.828	14:31:5.14	2.41 ± 0.27	$(1.07 \pm 0.09) \times (0.59 \pm 0.09)$, -88 ± 7	-11	61	W51d2
SMA4	19:23:39.756	14:31:5.37	1.40 ± 0.22	$(0.79 \pm 0.12) \times (0.49 \pm 0.13)$, -23 ± 21	-30	24	-

NOTE. — Resolved components of the east-west dust ridge in the SMA-Ext data. $\langle\phi_{\text{pol}}\rangle$ and $\sigma_{\phi_{\text{pol}}}$ are the mean and the standard deviation of the polarization position angles (ϕ_{pol}), respectively. Deconvolved sizes for SMA1 to SMA4 are obtained by fitting 2D-Gaussians.

The $870\ \mu\text{m}$ continuum emission is resolved in both SMA-SubC and SMA-Ext. With θ_{syn} of $4''$ (SMA-SubC), the $870\ \mu\text{m}$ continuum emission is elongated in the east-west (EW) direction with an extension toward the north (Figure 1b). This is consistent with the $2\ \text{mm}$ continuum map (Zhang et al. 1998) and the thermal NH_3 emission (Zhang & Ho 1995). With θ_{syn} of $0''.7$ (SMA-Ext), the EW ridge is further resolved into SMA1 to SMA4, as labeled in Figure 1a. The coordinates and flux densities of SMA1 to SMA4 are determined by fitting 2-D Gaussians. They are listed in Table 2.

The brightest $870\ \mu\text{m}$ continuum peak is SMA1, which is consistent with the location of the brightest peak at $7\ \text{mm}$ (Zapata et al. 2009) and at $2\ \text{mm}$ (Zhang et al. 1998). SMA2, SMA3 and SMA4 are resolved for the first time in the mm/submm regime. For SMA2, although there is no previous report of detection, it can be seen at $1.3\ \text{mm}$ (Figure 1 in Zapata et al. 2008). Associated with SMA3 is the UCHII region W51 d2, $0''.5$ to the south, and a NH_3 maser (Mauersberger et al. 1987; Wilson et al. 1991; Gaume et al. 1993). Among these 4 resolved SMA sources, SMA3 is the most evolved source due to its free-free emission, which suggests the existence of ionized gas. The existence of masers in SMA1 and SMA3 suggests that these two locations are active in star formation.

3.1.2. Flux Density and Mass

The flux density detected with SMA-SubC is $27 \pm 3\ \text{Jy}$. Comparing to the single dish measurement at the same location of $44\ \text{Jy}$ (Chrysostomou et al. 2002), about 60% of the flux density is recovered in SMA-SubC. The compact structures (SMA1 to SMA4) identified from SMA-Ext have a total flux density of $15 \pm 1\ \text{Jy}$ over the EW dust ridge. Comparing to the total emission of $44\ \text{Jy}$, these compact structures make for about 34% of the total emission. The majority of the emission is, thus, in the extended structure which is filtered out by the sampling of longer baselines.

The free-free continuum emission is $2.5\ \text{mJy}$ at $3.6\ \text{cm}$ toward W51 d2 (named as SMA3 in this paper; Gaume et al. 1993), and it will be $1.7\ \text{mJy}$ or $16\ \text{mJy}$ when extrapolated to $870\ \mu\text{m}$, assuming an optically thin spectral index (α) of -0.1 or an optically thick α of 0.6 , respectively. While the flux density of SMA3 is $2.4\ \text{Jy}$ at $870\ \mu\text{m}$, the contribution from free-free emission is negligible. The $870\ \mu\text{m}$ continuum emission along SMA1 to SMA4 is, thus, mainly from thermal dust emission. For the extended HII region W51 d, the flux density is $1\ \text{Jy}$ at $1.3\ \text{cm}$, and it will be $0.8\ \text{Jy}$ or $5\ \text{Jy}$ at $870\ \mu\text{m}$ assuming α of -0.1 or 0.6 , respectively. At this location, the detected intensity at $870\ \mu\text{m}$ with SMA-SubC is $\sim 5\ \text{Jy beam}^{-1}$. Thus, the traced extension to the north at $870\ \mu\text{m}$ could have a significant contribution from the free-

free emission, if this free-free emission is not optically thin between the wavelength of 1.3 cm and 870 μm .

The total gas mass, M_{gas} , can be estimated from the dust continuum, assuming a gas temperature of 100 K (Zhang et al. 1998), a dust opacity $\kappa_{\lambda=870\mu\text{m}} \propto \lambda^{-2} \approx 0.4 \text{ cm}^2 \text{ g}^{-1}$ (following the standard equation in Agladze et al. 1996), and a gas-to-dust ratio of 100. For SMA1, M_{gas} is $\sim 130 M_{\odot}$, roughly consistent with the value reported in Zhang et al. (1998) of $100 M_{\odot}$ and Zapata et al. (2008) of $90 M_{\odot}$. For SMA 2, SMA 3 and SMA 4, M_{gas} is 39, 36 and $21 M_{\odot}$, respectively. We note that the estimated mass can vary by a factor of a few due to the uncertainty in κ_{λ} , the assumed dust temperature, the gas-to-dust ratio and the distance to the source.

3.2. Dust Polarization

3.2.1. Morphology

The linear polarization is detected in most parts of the dust ridge (Figures 1b and 1c). The presented polarization segments were gridded every $0''.3$ for SMA-Ext and every $2'' \times 1''.8$ for SMA-SubC, which is about half of the synthesized beam in order to present the variations of the position angles (P.A.s). The detected polarization data above $2.5 \sigma_{I_p}$ for the SMA-Ext and above $2 \sigma_{I_p}$ for the SMA-SubC are listed in Table 3. We choose to set a $2\sigma_{I_p}$ threshold for the SMA-SubC in order to recover more polarization segments, where otherwise only 8 (out of 15) for SMA-SubC and 43 (out of 48) for SMA-Ext segments would remain with a $3\sigma_{I_p}$ limit.

In the SMA-SubC map (Figure 1b), there is a region without significant polarization about $2''$ north of SMA3. As zooming in with SMA-Ext, there are zones without significant polarization in between SMA1 and SMA2, between SMA2 and SMA3 and at the peak of SMA3 and SMA4. The areas without significant polarization near the intensity peaks and in between SMA1 and SMA2 may be due to complex underlying field geometries, as they appear in between two dramatically different PA regions. One example of a complex field in a region with low/no polarization detection is the W51 e2/e8 region. Observationally, the W51 e2 core was found to have low/no polarization in the 1.3 mm continuum with lower angular resolution ($3''$) by Lai et al. (2001). This core has actually been detected and resolved in polarization at 870 μm at higher angular resolution ($0.7''$) by Tang et al. (2009b).

3.2.2. Distribution Plots

The distributions of the polarization position angles (ϕ_{pol}) are shown in Figure 2a. In the shorter baseline data (SMA-SubC), the ϕ_{pol} are mainly in two ranges, namely around 50° and around -60° . As we will discuss in section 4.1, this bimodal-like distribution reflects a mirror symmetry in the polarization structure. The component at 50° is consistent with the single dish polarization measurement at 350 μm with an angular resolution of about $20''$ (Dotson et al. 2010). With smaller θ_{syn} (SMA-Ext), the dust ridge and polarization are further resolved and exhibit more structures. In the majority of the detected patches, values for ϕ_{pol} are around -50° with smooth variations within these areas (Figure 1c). The distribution for SMA-Ext is, consequently, peaking around -50° in Figure 2a. Near SMA2, the ϕ_{pol} are very

TABLE 3
POLARIZATION DATA DETECTED WITH THE SMA

$\Delta\text{R.A.}$ ($''$)	$\Delta\text{Dec.}$ ($''$)	P (%)	ϕ_{pol} ($^\circ$)	$\sigma_{\phi_{\text{pol}}}$ ($^\circ$)	I_p (mJy/b)	I (Jy/b)
Extended Track						
0.3	-0.3	1.8 ± 0.6	-58	10	9	0.48
0.0	-0.3	2.2 ± 0.5	-55	6	14	0.62
-0.3	-0.3	2.0 ± 0.6	-52	9	9	0.44
-2.7	-0.3	3.2 ± 0.8	-66	7	11	0.36
-3.0	-0.3	3.4 ± 0.6	-67	5	15	0.43
-3.3	-0.3	2.8 ± 0.7	-58	7	11	0.39
-3.6	-0.3	3.9 ± 0.8	-49	6	14	0.36
-3.9	-0.3	4.3 ± 1.0	-47	6	12	0.29
0.3	0.0	0.7 ± 0.2	-70	10	8	1.13
0.0	0.0	0.8 ± 0.2	-57	7	11	1.50
-0.3	0.0	0.9 ± 0.2	-47	8	10	1.17
-2.7	0.0	2.3 ± 0.6	-97	7	12	0.50
-3.0	0.0	1.2 ± 0.4	-83	8	10	0.80
-3.6	0.0	1.4 ± 0.4	-49	9	9	0.63
-3.9	0.0	2.4 ± 0.6	-41	8	11	0.45
-4.2	0.0	1.7 ± 0.7	-20	11	7	0.41
0.3	0.3	0.4 ± 0.1	-81	9	9	2.13
0.0	0.3	0.3 ± 0.1	-61	8	9	2.92
-0.3	0.3	0.5 ± 0.1	-49	7	11	2.30
-1.5	0.3	1.2 ± 0.3	-6	8	10	0.83
-1.8	0.3	2.0 ± 0.7	-0	10	8	0.39
-2.7	0.3	2.4 ± 0.6	85	7	12	0.49
-3.0	0.3	1.1 ± 0.3	82	8	10	0.85
-3.9	0.3	2.4 ± 0.6	-49	8	10	0.44
1.2	0.6	2.5 ± 0.9	-72	10	8	0.31
0.9	0.6	1.2 ± 0.4	77	10	8	0.69
0.6	0.6	0.6 ± 0.2	84	10	8	1.50
0.3	0.6	0.3 ± 0.1	-97	9	9	2.59
-1.2	0.6	0.6 ± 0.2	29	10	8	1.38
-1.5	0.6	1.5 ± 0.3	20	5	15	0.98
-1.8	0.6	3.0 ± 0.7	22	7	12	0.39
-3.0	0.6	3.1 ± 0.7	80	6	12	0.40
-3.3	0.6	1.8 ± 0.6	67	9	9	0.49
-3.6	0.6	2.7 ± 0.9	-69	9	9	0.32
-4.2	0.6	1.5 ± 0.5	-70	9	9	0.58
0.9	0.9	1.8 ± 0.5	83	8	10	0.55
0.6	0.9	0.8 ± 0.3	-97	9	9	1.05
0.3	0.9	0.5 ± 0.2	-83	9	9	1.63
-1.2	0.9	1.1 ± 0.3	35	7	11	1.03
-1.5	0.9	3.6 ± 0.5	36	4	19	0.53
0.6	1.2	3.0 ± 0.9	-67	8	10	0.32
0.3	1.2	2.0 ± 0.6	-81	8	10	0.49
0.0	1.2	1.2 ± 0.4	94	10	8	0.68
-0.9	1.5	2.6 ± 0.8	63	8	9	0.37
-2.1	4.8	1.6 ± 0.6	-22	10	8	0.49
-1.8	5.1	1.6 ± 0.6	-43	10	8	0.50
-2.1	5.1	1.9 ± 0.6	-25	9	9	0.45
Subcompact Track						
0.0	-2.0	0.9 ± 0.3	-69	9	47	5.15
-1.8	-2.0	1.0 ± 0.3	-53	7	57	5.70
-3.6	-2.0	1.1 ± 0.4	-41	10	43	3.83
-5.4	-2.0	0.8 ± 0.5	-27	17	25	3.04
1.8	0.0	0.9 ± 0.3	-74	9	47	5.14
0.0	0.0	0.7 ± 0.1	-62	5	86	12.15
-1.8	0.0	0.7 ± 0.1	-50	5	80	12.07
-3.6	0.0	0.7 ± 0.2	-34	9	47	6.85
-5.4	0.0	0.8 ± 0.3	-15	13	34	4.33
1.8	2.0	1.3 ± 0.4	-88	9	50	3.93
0.0	2.0	0.7 ± 0.2	-80	7	61	9.05
0.0	4.0	1.3 ± 0.6	74	13	34	2.60
-1.8	4.0	1.4 ± 0.5	56	10	43	3.05
-3.6	4.0	2.0 ± 0.7	47	10	42	2.10
-5.4	4.0	2.9 ± 1.2	41	12	35	1.21

NOTE. — Offset in Right Ascension ($\Delta\text{R.A.}$) and offset in Declination ($\Delta\text{Dec.}$) with respect to the phase center ($19^{\text{h}}23^{\text{m}}40.05^{\text{s}}$, $14^{\circ}31'5''0$)_{J2000}, polarization percentage (P), position angle of polarization (ϕ_{pol}), the uncertainty of the position angle of polarization ($\sigma_{\phi_{\text{pol}}}$), polarization intensity (I_p), and Stokes I intensity (I). I_p and I are in units of mJy beam^{-1} (mJy/b) and Jy beam^{-1} (Jy/b), respectively. Data listed are above $2.5\sigma_{I_p}$ and above $2\sigma_{I_p}$ for SMA-Ext and SMA-SubC, respectively.

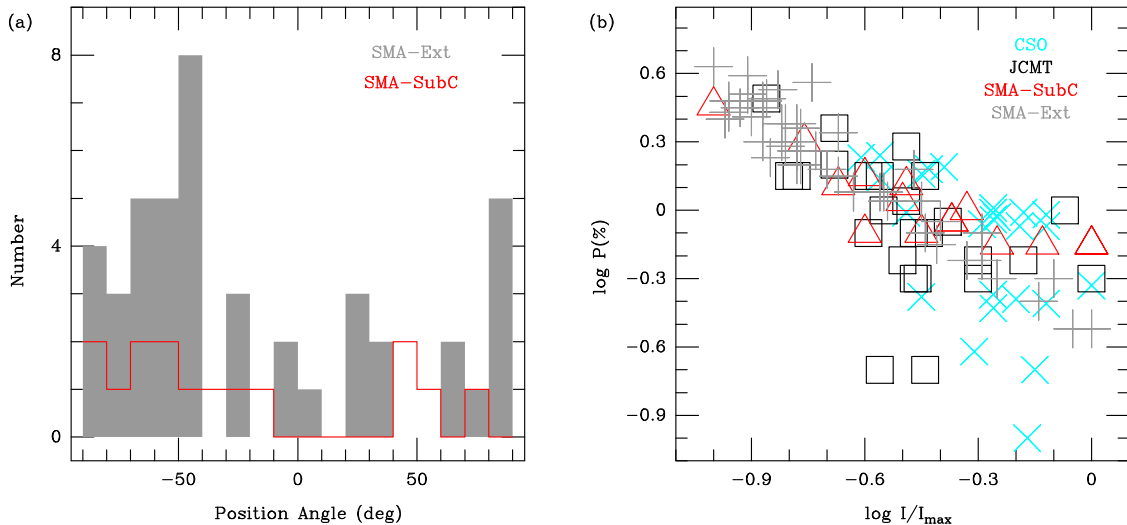


FIG. 2.— (a) Distributions of detected polarization position angles (ϕ_{pol}). (b) Polarization percentage ($P\%$) versus normalized Stokes I dust intensity, I/I_{max} .

different from the ϕ_{pol} at the other positions. The ϕ_{pol} of these segments are more perpendicular to the intensity gradients at these positions (Figure 1c). Since there are no reported ongoing star formation activities here, the origin of this abrupt change in ϕ_{pol} from SMA1 to SMA2 and to SMA3 is not clear. The component with ϕ_{pol} of 50° seen in the SMA-SubC map is not seen in the SMA-Ext map (Figure 1c). This suggests that this component originates from extended structures and is not sampled in the SMA-Ext data.

A log-log plot of the polarization percentage (P) versus the normalized intensity is shown in Figure 2b. $P(\%)$ is in the range of <1 to 4.5% and the mean $P(\%)$ is 1.81% and 1.07% for the SMA-Ext and SMA-SubC, respectively. There is a general trend for both our high-angular-resolution data and the single dish data from the CSO and the JCMT: P decreases with larger intensity. Numerical simulations have shown that such anti-correlations can be due to a more complex ϕ_{pol} -structure in dense regions (Falceta-Gonçalves et al. 2008).

4. DISCUSSION

In this section we discuss the different morphologies in the dust emission with its associated B field from 4 different scales/layers. The larger scale data (shown in Figures 3a and 3b) are from the single dish by CSO (Hertz, Dowell et al. 1998) at $350 \mu\text{m}$ (Dotson et al. 2010) at a scale of 3 pc and by JCMT (SCUBA, Holland et al. 1998) at $850 \mu\text{m}$ (Chrysostomou et al. 2002) at a scale of 2 pc. The smaller scale data are from our SMA-SubC at a scale of 0.3 pc and from SMA-Ext at a scale of 60 mpc at $870 \mu\text{m}$ (Figure 3c). The position angle of the magnetic field (ϕ_{B}) is obtained by rotating the detected ϕ_{pol} by 90° . We also provide a quantitative analysis in support of the observational description in section 4.2. We conclude in section 4.3 with a schematic scenario of the magnetic field observations so far in the W51 North region.

4.1. SMA high-resolution magnetic field morphologies

The dust continuum morphology in the SMA-SubC shows regular contours with an extension to the west. These contours show some symmetries along an EW

axis around $\Delta\text{Dec.}=0''$ (Figure 3c). Similarly, the detected polarization segments reveal a north-south symmetry (upper and lower planes) along the same axis. Assuming flux-freezing with the gas mostly moving along the field lines, the combined observed symmetry patterns (in the dust continuum and the field morphologies) are suggestive to find mass accumulations mostly along the symmetry axis. Indeed, the detected cores (SMA1 to SMA4) in the SMA-Ext data (Figure 3c) are mostly aligned on an EW axis at the above declination. Thus, the observed field configuration on the ~ 0.3 pc scale (SMA-SubC) appears to be channeling and aligning material, which is detected as denser cores on a ~ 60 mpc scale (SMA-Ext) once the extended emission is filtered out.

Unlike the symmetric field configuration on the ~ 0.3 pc scale, the smaller individual cores on the ~ 60 mpc scale show very different field morphologies. SMA1 exhibits ϕ_{B} orientations roughly comparable to that of the one corresponding segment of the subcompact data (Figure 3c). The morphology possibly also shows a hint of gravity dragging in the B field lines toward the center. The patch of segments in SMA2 is rather orthogonal to the SMA-SubC segment next to it. SMA3 and SMA4 show again a more closer alignment with the single SMA-SubC segment but with some deviations up to about 45° . Thus, within one resolution element of the SMA-SubC data (where neighboring segments along the symmetry axis show only little changes in orientation), the detected ϕ_{B} in the SMA-Ext data show changes in orientation of up to 90° .

The B morphology associated with SMA1 is particularly interesting. As mentioned in section 1, collapsing signatures and a rotating molecular ring have been reported toward SMA1 (Sollins et al. 2004; Zapata et al. 2008, 2009). The detected pinched B field morphology associated with SMA1 is, therefore, consistent with the picture of the B field lines being dragged by inward motions and/or the rotation of the molecular ring.

Despite the very different field orientations in SMA1 to SMA4, the ϕ_{B} in these cores all reveal a common

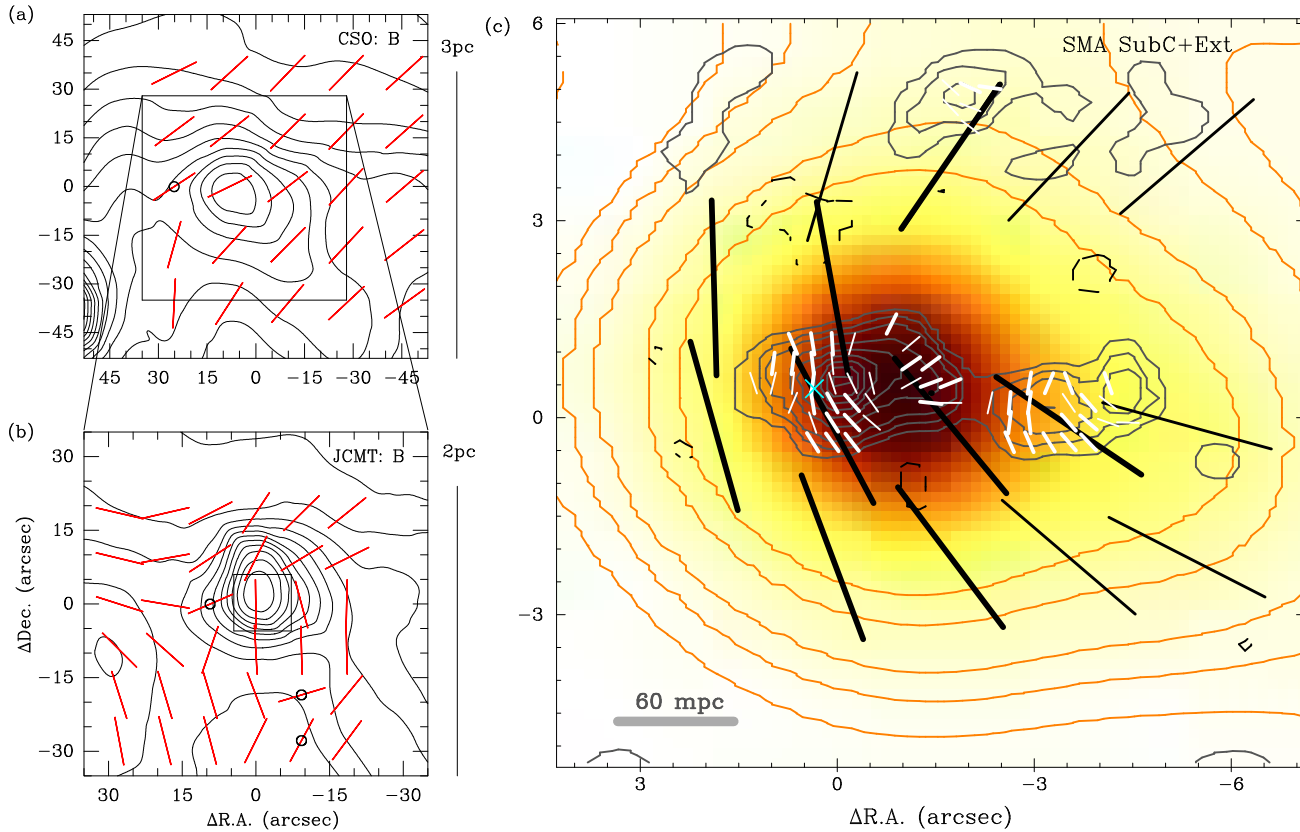


FIG. 3.— The B field map in W51 North obtained from four different scales and/or layers (see also Figure 7): 3 pc scale by HERTZ on the CSO in (a) and 2 pc scale by SCUBA on the JCMT in (b), and sub-pc scale by the SMA-SubC (black segments) and by SMA-Ext (white segments) in (c). In (a) and (b), the contours and the red segments label the continuum emission and the B field orientations, respectively. The small circles mark the data with larger uncertainties in position angles (15° to 30°) as compared to the other data points. The contours start from and step in 5% of the peak intensity detected in CSO of 694 Jy and in JCMT of 44 Jy in (a) and (b), respectively. The black square in panel (a) marks the mapping area in panel (b), and the one in panel (b) marks the mapping area in panel (c). In (c), the continuum emission traced with the SMA-SubC is shown in orange contours and in color scale, and the contours are 3, 6, 10, 20, 30 \times 0.19 (Jy beam $^{-1}$). The continuum emission detected in the SMA-Ext is plotted in grey contours in the same level as in Figure 1. The cyan \times marks the center of the rotating toroid detected by Zapata et al. (2009).

trend: the field segments tend to be aligned with the orientations of the dust continuum intensity gradients, $\phi_{\nabla I}$, in many locations⁶. In section 4.2, we will have a more quantitative analysis on this correlation.

4.2. Quantitative Analysis

Figures 4a to 4d show the dust emission maps overlaid with the magnetic field segments (red) and the intensity gradient segments (blue). Inspired by the close alignment of the position angles of the intensity gradients, $\phi_{\nabla I}$, and the position angles of the B field, ϕ_B , we apply further analyses in this subsection.

4.2.1. Correlation of $\phi_{\nabla I}$ and ϕ_B

We first compare the correlation of $\phi_{\nabla I}$ and ϕ_B in these 4 data sets. The correlation plots are shown in Figure 5. The uniformity of the B field traced with the CSO is apparent here with a large group of data points scattering around ϕ_B of 120° . Except for the CSO data, the correlation between $\phi_{\nabla I}$ and ϕ_B can be seen by eye.

The correlation is further analyzed quantitatively using Pearson's correlation coefficient, \mathcal{C} . The uncertainties in

⁶ The dust intensity gradients are orthogonal to the dust emission contours (in the plane of sky). The resulting position angles, $\phi_{\nabla I}$, are defined in the range of 0° to 180° .

the correlation coefficient (the standard deviation), σ_C , are estimated using a Monte-Carlo approach where errors in both ϕ_B and $\phi_{\nabla I}$ are propagated through the calculation. Gaussian distributions of the ϕ_B ($= \phi_{\text{pol}} + 90^\circ$) uncertainties at two sigma level, i.e. 2 times the $\sigma_{\phi_{\text{pol}}}$ term in Table 3, are adopted. Gaussian distributions with mean uncertainties of $\sim 3^\circ - 5^\circ$ – which is the result after interpolating between Stokes I values in order to calculate gradients – are used for the $\phi_{\nabla I}$ uncertainties. Resulting values of σ_C are in the range of 0.02 to 0.08.

As listed in Table 4, \mathcal{C} is highest in the highest resolution data (SMA-Ext), being 0.88 ± 0.01 , suggesting that the correlation between $\phi_{\nabla I}$ and ϕ_B is tightest in the structures revealed with SMA-SubC, the \mathcal{C} value is 0.78 ± 0.03 . For SMA-SubC, the \mathcal{C} values for the CSO and the JCMT data are 0.81 ± 0.03 and 0.70 ± 0.02 , respectively. We further derive the \mathcal{C} values for the CSO and the JCMT data for two separated regions: the core and the region outside of the core. The \mathcal{C} values are larger in the cores, being 0.88 ± 0.04 and 0.73 ± 0.02 in the CSO and JCMT data, respectively. This is similar to the high \mathcal{C} value in SMA-Ext, further confirming that the $\phi_{\nabla I}$ and ϕ_B correlation is higher in the cores. Outside of the core region, the \mathcal{C} values are generally smaller (0.59 ± 0.04 for CSO and 0.66 ± 0.02 for JCMT), and the correlation

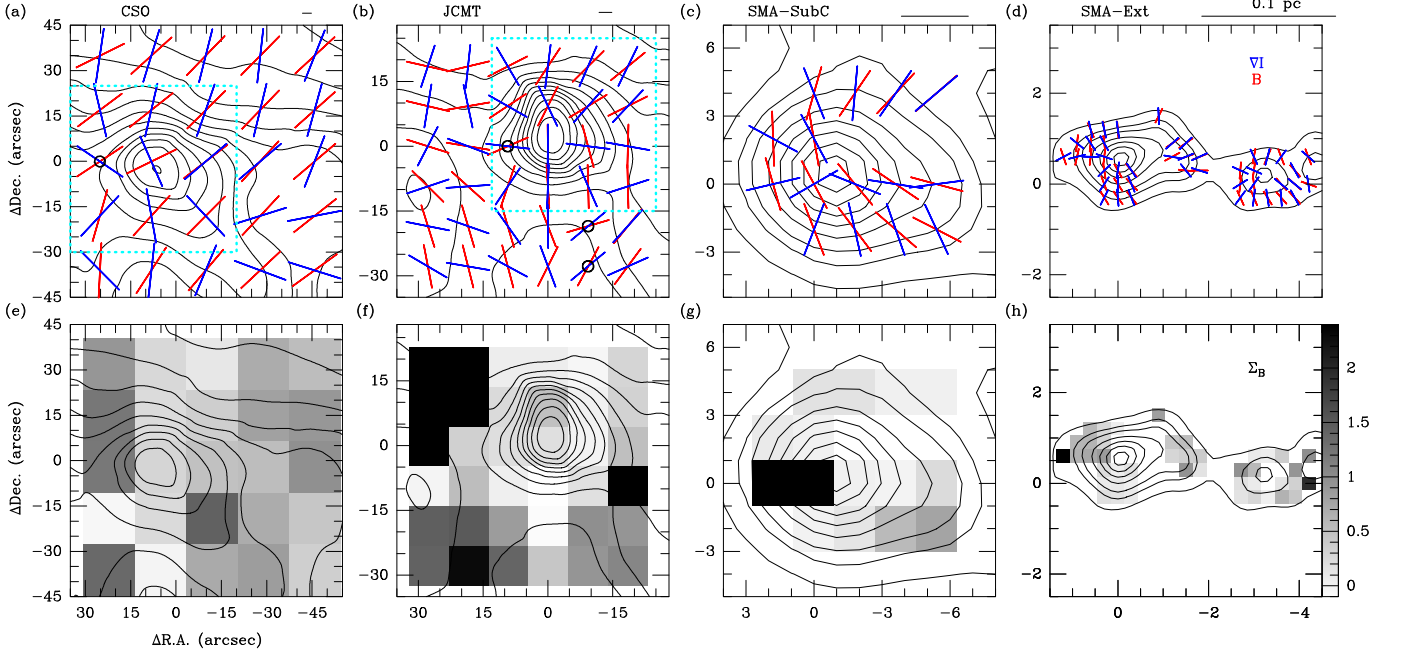


FIG. 4.— Comparison of the four different field morphologies observed with Hertz on the CSO in (a,e), SCUBA on the JCMT in (b,f), the SMA-SubC in (c,g) and the SMA-Ext in (d,h). In the top row (a-d), the total intensity (contours), the B field (red segments) and the intensity gradient (blue segments) orientations are shown. The derived force ratios of the B field to the gravity, Σ_B , are shown in grey scale in the bottom row panels (e-h). Darker colors indicate that the B field is dominant ($\Sigma_B > 1$). Lighter colors indicate that the B field plays a minor role ($\Sigma_B < 1$). Cyan squares mark the core areas used in Table 4. A segment representing a 0.1 pc scale-length is plotted in the upper-right corners for a reference. The small black circles in the panels (a) and (b) mark the data with magnetic field P.A. uncertainties between 15 to 30°.

TABLE 4
ANALYSIS SUMMARY

Parameters	CSO			JCMT			SMA-SubC	SMA-Ext		
$\theta_{(\text{syn})}$ (")	20			9.3			4	0.7		
λ (μm)	350			850			870	870		
B morphology	uniform			uniform patches, changes in large scale			shaped, cometary-like, N-S mirror symmetry	shaped, possibly hourglass-like		
	all	core ^a	out ^b	all	core ^a	out ^b	all	all	core1 ^c	core2 ^c
\mathcal{C}	0.81	0.88	0.59	0.70	0.73	0.66	0.78	0.88	0.89	0.86
$\sigma_{\mathcal{C}}$	0.06	0.08	0.08	0.03	0.04	0.03	0.05	0.02	0.02	0.03
$\langle \Delta\phi_B \rangle$	12°	-	-	43°	-	-	43°	39°	-	-
$\sigma_{ \Delta\phi_B }$	13°	-	-	27°	-	-	26°	26°	-	-
$\langle \delta \rangle$	40°	51°	34°	44°	38°	48°	37°	35°	34°	36°
$\sigma_{ \delta }$	22°	29°	15°	27°	28°	26°	26°	24°	26°	23°
$\langle \Sigma_B \rangle$	0.71	0.69(0.59)	0.72	1.17	0.42(0.27)	1.84	0.47(0.18)	0.48(0.38)	0.47(0.37)	0.48(0.39)

NOTE. — Statistical quantities derived using the position angles of the intensity gradient ($\phi_{\nabla I}$) and the position angles of the magnetic field (ϕ_B). $\theta_{(\text{syn})}$ and λ are the angular resolution and the wavelength of the traced emission, respectively. \mathcal{C} is the Pearson's correlation coefficient between ϕ_B and $\phi_{\nabla I}$, and its standard deviation is given by $\sigma_{\mathcal{C}}$. $\langle |\Delta\phi_B| \rangle$ and $\sigma_{|\Delta\phi_B|}$ are the mean difference of ϕ_B of polarization pairs and the standard deviation of the difference, respectively. $\langle |\delta| \rangle$ and $\sigma_{|\delta|}$ is the mean of the absolute difference between ϕ_B and $\phi_{\nabla I}$ and its standard deviation, respectively. $\langle \Sigma_B \rangle$ is the mean of the ratio of the magnetic field force to gravitational force (Σ_B), which is calculated with the method introduced in Koch et al. (2012a). Values after removing the outliers are listed in parenthesis.

(a) Values derived using the pixels marked within the cyan square in Figure 4.

(b) Values derived using the pixels outside the cyan square in Figure 4 (named as outside of the core region in the text).

(c) Core1 and core2 refers to SMA1,2 and SMA3,4, respectively.

is worse. It is systematic that both the CSO and the JCMT data show a difference in \mathcal{C} between the core and the outside-the-core region. We will propose a physical interpretation for such a change in \mathcal{C} in section 4.2.2.

In addition to the $\phi_{\nabla I}$ - ϕ_B plot, we also compare the distribution of the angle difference, ϕ_{δ} , between ϕ_B and $\phi_{\nabla I}$ (Figure 6a). It is important to note that all the distributions are non-Gaussian, i.e., the differences in the magnetic field and intensity gradient orientations are not

only due to a measurement uncertainty, but point toward a more fundamental physical interpretation as explored in Koch et al. (2012a).

The differences of individual pairs of field segments over an observed map are also compared. The histograms in Figure 6b display $|\Delta\phi_B| \equiv |\phi_{B,i} - \phi_{B,j}|$ for all possible pairs of segments i and j in a map. A systematic difference is apparent between the CSO data and the other 3 data sets. The CSO distribution peaks at small values,

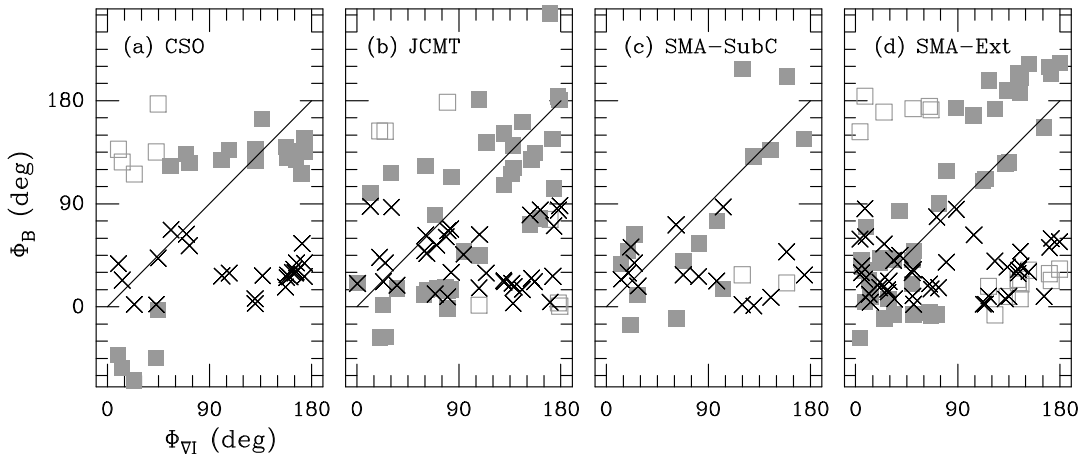


FIG. 5.— Position angles of the intensity gradient orientations, $\phi_{\nabla I}$, and the B field orientations, ϕ_B , in solid squares. Crosses mark the absolute differences between $\phi_{\nabla I}$ and ϕ_B . In order to properly display their correlations, the ϕ_B is re-defined beyond the 0° - 180° range (filled squares above 180° and below 0°) for ambiguous situations; i.e., a pair of position angles of 175° and 5° is displayed as 175° and 185° . The hallowed squares mark their original data points. Note that this re-definition does not change the correlation in any way, but is merely a consequence of the 180° ambiguity in the range of position angles. The straight line represents a perfect correlation.

with an average change in orientation $\langle |\Delta\phi_B| \rangle = 12^\circ$, whereas the other distributions are close to flat with average changes around 40° (Table 4). This reflects the visual impression that the field is mostly uniform in orientation in the CSO map at ϕ_B of 120° . In the other maps, the field orientations seem to be more significantly shaped and overcome by other forces, erasing the original likely uniform orientation of the field. Thus, one might conclude that on the largest scales, a uniform field morphology points to a more significant role of the magnetic field.

4.2.2. Application of the Polarization - Intensity Gradient Method

In this subsection, we apply the new polarization-intensity gradient method to derive the force ratio (Σ_B) map of the magnetic field to the gravitational force (see Koch et al. 2012a, for the development of the method). The derivation of Σ_B makes use of $|\phi_\delta|$ in combination with an additional angle between $\phi_{\nabla I}$ and the local gravity direction. This local gravity direction is calculated from the positions of the gravity centers which are identified with the emission peaks in a map⁷. For SMA-Ext, two gravity centers are defined, namely SMA1 and SMA3, around which most of the polarization is detected. Figures 4e to 4h show maps of the force ratio Σ_B . Values averaged over the map, $\langle \Sigma_B \rangle$, are listed in Table 4. The uncertainties of the derived ratios depend on several factors, such as the ϕ_{pol} uncertainties and the positions of the gravity centers in a map. Adopting uncertainties like in the previous section for \mathcal{C}_{err} , typical errors in Σ_B are $\sim 5\%$ for core-like structures like in SMA-Ext. The errors can grow to $\sim 20\%$ for larger scale field morphologies where gravity centers are less defined. Averaging Σ_B over a larger area (cores, outside-core regions) will

⁷ For the original derivation of the force ratio Σ_B we refer the reader to Koch et al. (2012a). Σ_B is found from an MHD force equation, comparing the field tension force F_B and the gravitational force F_G via measurable angles: $\Sigma_B = F_B/F_G = \sin\psi/\sin\alpha$. The angle ψ is defined by the intensity gradient and the direction of gravitational force. The angle α is between the intensity gradient and the originally detected polarization orientations.

typically lead to errors of a few percents.

The $\langle \Sigma_B \rangle$ values of the large-scale observations with the CSO and the JCMT are around 0.71 and 1.17 when averaged over the entire area, respectively. If we separate the values into core region and outside-the-core region, $\langle \Sigma_B \rangle$ is 0.69 (~ 0.59 if outliers are removed) and 0.72 for CSO in the core and outside, respectively. For JCMT, the variation is more dramatic, being 0.42 (0.27 if outliers are removed) and 1.84 for the core and the region outside of the core, respectively. We, thus, find that Σ_B tends to be smaller for the cores than in the areas outside of the cores. The smaller-scale SMA data also show a reduced magnetic field significance with $\langle \Sigma_B \rangle \sim 0.5$. Generally, closer to and around the emission peaks, the force ratios seem to be smaller. This implies that on these scales the magnetic field is more shaped and dominated by gravity. In the regions outside of the core, the ratios are larger or the field is even dominating gravity ($\Sigma_B > 1$ for JCMT).

This change in the role of the magnetic field based on the force ratio Σ_B might provide a physical explanation of the change of the correlation coefficient \mathcal{C} described in section 4.2.1. The tighter correlation of $\phi_{\nabla I}$ and ϕ_B in the cores suggests that the B field lines are mainly dragged by gravity and, consequently, align with the intensity gradient. Therefore, quantitatively, the B field is indeed of minor importance in the cores. We emphasize that the \mathcal{C} value is purely statistical without any physical assumptions. In contrast, the Σ_B value is calculated by identifying various terms in an ideal MHD force equation in an observed Stokes I and dust polarization map. These two approaches are, thus, largely independent. They, nevertheless, seem to lead to a consistent picture where the magnetic field significance is reduced in the core regions.

4.3. Global Picture of the Magnetic Field in W51 North

Figure 7 schematically summarizes the 4 magnetic field observations analyzed in the previous sections. Each panel represents a plane-of-sky projected observation of the CSO, JCMT, SMA-SubC and SMA-Ext, respectively, where a subsequently higher-angular-resolution observation is zooming in on a previous one. In this

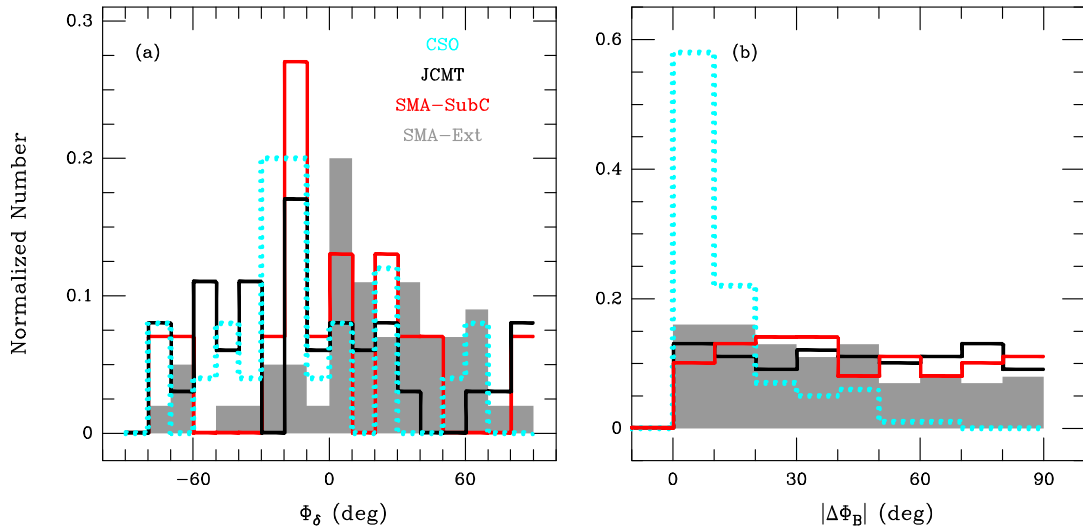


FIG. 6.— (a) Histograms of the differences in position angles between the B field and the intensity gradient (ϕ_δ). (b): Histograms of the absolute values of the differences in position angles of the polarization pairs ($|\Delta\phi_B|$).

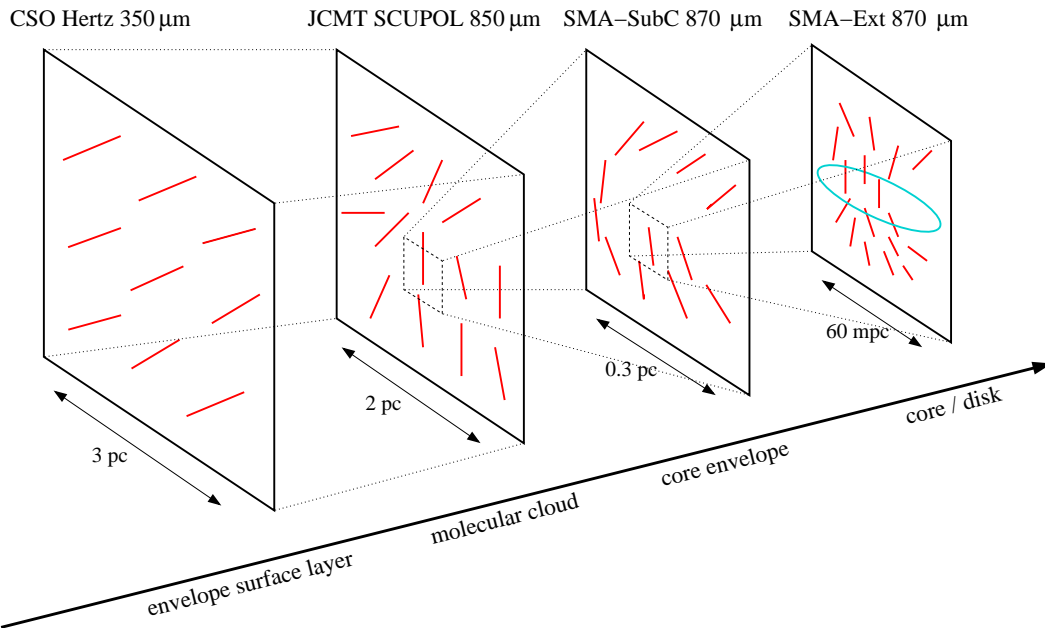


FIG. 7.— Schematic illustration of the different magnetic field structures sampled at various depths along the line of sight and at different scales. The cyan ellipse marks the location of the collapsing and rotating molecular core found in Zapata et al. (2009).

sequence of observations, field morphologies are sampled from a 3 pc scale down to a 60 mpc physical scale.

These four panels represent the field geometry from different layers or from different scales in the W51 North region. For the CSO image, the flux from an optically thick $20''$ (the CSO resolution) source at a rotational temperature T of 15 K will be 270 Jy, and 760 Jy at $T=30$ K. This is in the range of Stokes I intensity in the observed region (Dotson et al. 2010). We note that the rotational temperature of W51 N is 45 K as traced by ammonia lines (Zhang & Ho 1997) and the detected structure is $\sim 10''$. A decreasing temperature from the UCHII region to the outer surrounding gas is further proposed by Zhang et al. (1998). Thus, the gas temperature within a $20''$ beam is unlikely to be much higher than 30 K. Unless the temper-

atures are substantially higher, the average opacity must be of order 1. Furthermore, the observed polarization arises from the difference in emissivity of dust grains. In an optically thick medium, the polarization comes from upper layers. We then expect the field morphology to rather result from an upper surface layer than from the deeper embedded core. This is the first panel in Figure 7 which is labeled as *envelope surface layer*. The field is mostly uniform here, with a single orientation still reflecting the largest scale field structure. The field-to-gravity force ratio is relatively large (~ 0.7 , Table 4) and rather uniform with only a minor difference between core and outside-core region (Figure 4e). The correlation \mathcal{C} , between field and intensity gradient orientations, is poorest outside the core ($\mathcal{C} \sim 0.59$). This all is suggestive of a

magnetic field that is still retaining its tension force in this surface layer.

The JCMT 850 μm observation – with a higher resolution and reaching deeper inside the core – shows still some uniform patches in field morphology, but also clearly displays changing field orientations in the core. In this next deeper layer (labeled as *molecular cloud* in Figure 7), the field ratio shows a clear difference between core (~ 0.4) and outside-core region (> 1 , Figure 4f). This might indicate that gravity is overcoming the field tension in the core area, whereas the field remains significant at larger distances, possibly even holding back material from further accreting onto the core. Thus, the CSO and JCMT observations, despite covering similar areas, seem to sample different depths where the magnetic field seems to play different roles.

The SMA-SubC 870 μm observation is akin to zooming in on the JCMT observation. The force ratio Σ_B and the correlation \mathcal{C} are comparable to the JCMT values. This observation seems to further sharpen the JCMT core, removing some of the extended emission (third panel labeled as *core envelope* in Figure 7). In addition to the JCMT observation (which already shows a core being dominated by gravity), the North-South symmetry in the SMA-SubC field morphology provides a hint for yet another role of the magnetic field: material can be channeled along the field lines onto an east-west axis. Finally, the SMA-Ext data with sub-arcsecond resolution clearly resolve the $\sim 0.3\text{pc}$ structure into 4 cores (fourth panel labeled as *core/disk* in Figure 7). Distinct morphologies are found for individual cores, with all cores consistently showing the tightest correlations (~ 0.9) and clearly low force ratios (~ 0.4). At this scale, an hourglass-like morphology is becoming visible.

In summary, we thus propose a schematic scenario in Figure 7, for the change in the B field, from the largest scale envelope surface layer down to the scale where a collapsing core is being revealed. The scenario described above emerges from visual impressions from the field morphologies, combined with a quantitative analysis from correlations and force ratios.

Finally, it is interesting to remark that *generally* the correlation coefficients \mathcal{C} are found to be larger in the cores than outside of the cores in all 4 scales and/or layers. The mean ϕ_δ (the difference between $\phi_{\nabla I}$ and ϕ_B) and its standard deviation in the cores tend to be smaller than the ones outside the cores. Both the analyses of \mathcal{C} and ϕ_δ suggest that ϕ_B has a tighter correlation with $\phi_{\nabla I}$ in the cores. Similarly, the force ratio of the B field strength and the gravity (Σ_B) in these 4 data sets also reveal a common trend: Σ_B tends to be smaller in the cores than outside the cores, suggesting that gravity is generally playing a more important role within the cores. As already quantified and observed for other sources (Koch et al. 2012b), we can thus consistently confirm that the magnetic field significance systematically decreases toward the cores for various physical scales.

5. CONCLUSION AND SUMMARY

We present new high-resolution SMA dust polarization observations toward the molecular cloud W51 North. Beyond the polarization imaging we also apply new analysis techniques providing insight into the role and importance

of the magnetic field. Furthermore, we make the first attempt to present a magnetic field picture from the largest scales (3 pc) – from previously published CSO and JCMT data – to the SMA detected collapsing cores ($\sim 60\text{ mpc}$). The key points are summarized in the following.

1. Our new SMA high-resolution observations in the subcompact (SMA-SubC, angular resolution θ_{syn} of $4''$) and extended (SMA-Ext, θ_{syn} of $0''.7$) array configurations clearly detect and resolve the dense structures in W51 North. With the observed thermal dust Stokes I continuum emission at a wavelength of $870\ \mu\text{m}$, four dense cores, SMA1 to SMA4, are resolved in an east-west dust ridge.
2. The polarized thermal continuum at $870\ \mu\text{m}$ is detected and resolved with an angular resolution up to $0''.7$ for the first time with the SMA. The polarization percentage P ranges from 1 % to 4 %. P is found to decrease with higher intensity for both the SMA-SubC and SMA-Ext data. This trend is also largely identical to the larger scale CSO and JCMT polarization data.
3. The observed magnetic field configuration on the $\sim 0.3\ \text{pc}$ scale with the SMA-SubC shows some mirror-symmetry features from North to South. Here, the field lines might be channeling and aligning material from both North and South. At a $\sim 60\ \text{mpc}$ scale resolution observed with the SMA-Ext, dense cores are, indeed, detected along the east-west mirror symmetry axis. Smooth changes in field morphologies are found within individual cores, whereas large overall changes in position angles can occur in between the cores.
4. A correlation between dust intensity gradient position angles ($\phi_{\nabla I}$) and magnetic field position angles (ϕ_B) is found in the CSO, JCMT and both SMA data sets. This correlation is further analyzed quantitatively. A systematically tighter correlation between $\phi_{\nabla I}$ and ϕ_B is found in the cores, whereas at larger distances the correlation decreases.
5. Magnetic field to gravity force ratio (Σ_B) maps are derived using the newly developed polarization-intensity gradient method (Koch et al. 2012a). In this method, Σ_B is quantified by measuring angles that reflect the resulting forces shaping the dust Stokes I and magnetic field morphologies. We find that the force ratios tend to be small ($\Sigma_B \lesssim 0.5$) in the cores in all 4 data sets. In regions outside of the cores, the ratios increase or the field is even dominating gravity ($\Sigma_B > 1$). This possibly provides a physical explanation of the tightening correlation between $\phi_{\nabla I}$ and ϕ_B in the cores: the more the B field lines are dragged and aligned by gravity, the tighter the correlation is. Intuitively, in such a scenario one expects gravity to play an increasingly dominating role. The analysis via the force ratio Σ_B seems to consistently confirm this expectation. We stress that correlation and Σ_B are independent approaches. They, nevertheless, seem to reveal a matching picture.

6. Interpreting the four polarization observations covering different physical scales, we propose a schematic scenario for the magnetic field in W51 North (Figure 7). In the largest envelope surface layer (CSO), the field has kept much of its tension force. In the deeper-layer JCMT observation, gravity has overcome the magnetic field in the core whereas in the outside the field tension is significant, capable of holding back material against gravity. Both higher-resolution SMA observations show gravity dominating the field tension. In SMA-SubC, the field is possibly channeling material from

North and South onto an east-west axis. In SMA-Ext, four higher-resolution cores are aligned in an east-west axis, with a field morphology pointing toward hourglass-like structures as expected in a core/disk system.

This research was supported by NSC grants NSC99-2119-M-001-002-MY4 and NSC98-2119-M-001-024-MY4. This work was supported by Programme National de Physique Stellaire (PNPS) and Programme National de Physique Chimie du Milieu Interstellaire (PCMI) from INSU/CNRS.

REFERENCES

- Agladze, N. I., Sievers, A. J., Jones, S. A., Burlitch, J. M., & Beckwith, S. V. W. 1996, *ApJ*, 462, 1026
- Barbosa, C. L., Blum, R. D., Conti, P. S., Daminieli, A., & Figueredo, E. 2008, *ApJ*, 678, L55
- Cho, J., & Lazarian, A. 2005, *ApJ*, 631, 361
- Chrysostomou, A., Aitken, D. K., Jenness, T., Davis, C. J., Hough, J. H., Curran, R., & Tamura, M. 2002, *A&A*, 385, 1014
- Crutcher, R. M. 1999, *ApJ*, 520, 706
- Dotson, J. L., Vaillancourt, J. E., Kirby, L., Dowell, C. D., Hildebrand, R. H., & Davidson, J. A. 2010, *ApJS*, 186, 406
- Dowell, C. D., Hildebrand, R. H., Schleuning, D. A., Vaillancourt, J. E., Dotson, J. L., Novak, G., Renbarger, T., & Houde, M. 1998, *ApJ*, 504, 588
- Draine, B. T., & Weingartner, J. C. 1996, *ApJ*, 470, 551
- . 1997, *ApJ*, 480, 633
- Eisner, J. A., Greenhill, L. J., Herrnstein, J. R., Moran, J. M., & Menten, K. M. 2002, *ApJ*, 569, 334
- Falceta-Gonçalves, D., Lazarian, A., & Kowal, G. 2008, *ApJ*, 679, 537
- Falgarone, E., Troland, T. H., Crutcher, R. M., & Paubert, G. 2008, *A&A*, 487, 247
- Fish, V. L., & Reid, M. J. 2006, *ApJS*, 164, 99
- Gaume, R. A., Johnston, K. J., & Wilson, T. L. 1993, *ApJ*, 417, 645
- Genzel, R., et al. 1981, *ApJ*, 247, 1039
- Girart, J. M., Rao, R., & Marrone, D. P. 2006, *Science*, 313, 812
- Greaves, J. S., Murray, A. G., & Holland, W. S. 1994, *A&A*, 284, L19
- Hennebelle, P., Commerçon, B., Joos, M., Klessen, R. S., Krumholz, M., Tan, J. C., & Teyssier, R. 2011, *A&A*, 528, A72
- Hildebrand, R. H. 1988, *QJRAS*, 29, 327
- Ho, P. T. P., Moran, J. M., & Lo, K. Y. 2004, *ApJ*, 616, L1
- Holland, W. S., Cunningham, C. R., Gear, W. K., Jenness, T., Laidlaw, K., Lightfoot, J. F., & Robson, E. I. 1998, in *Society of Photo-Optical Instrumentation Engineers (SPIE) Conference Series*, Vol. 3357, Society of Photo-Optical Instrumentation Engineers (SPIE) Conference Series, ed. T. G. Phillips, 305–318
- Imai, H., Watanabe, T., Omodaka, T., Nishio, M., Kameya, O., Miyaji, T., & Nakajima, J. 2002, *PASJ*, 54, 741
- Koch, P. M., Tang, Y.-W., & Ho, P. T. P. 2012a, *ApJ*, 747, 79
- . 2012b, *ApJ*, 747, 80
- Kowal, G., Lazarian, A., & Beresnyak, A. 2007, *ApJ*, 658, 423
- Kraemer, K. E., Jackson, J. M., Deutsch, L. K., Kassis, M., Hora, J. L., Fazio, G. G., Hoffmann, W. F., & Dayal, A. 2001, *ApJ*, 561, 282
- Lai, S.-P., Crutcher, R. M., Girart, J. M., & Rao, R. 2001, *ApJ*, 561, 864
- Lazarian, A. 2000, in *Cosmic Evolution and Galaxy Formation: Structure, Interactions, and Feedback*, ed. J. Franco, L. Terlevich, O. López-Cruz, & I. Aretxaga, Vol. 215, 69
- Lazarian, A., & Hoang, T. 2007, *ApJ*, 669, L77
- Mac Low, M.-M., & Klessen, R. S. 2004, *Reviews of Modern Physics*, 76, 125
- Matthews, B. C., McPhee, C. A., Fissel, L. M., & Curran, R. L. 2009, *ApJS*, 182, 143
- Mauersberger, R., Henkel, C., & Wilson, T. L. 1987, *A&A*, 173, 352
- Okamoto, Y. K., Kataza, H., Yamashita, T., Miyata, T., & Onaka, T. 2001, *ApJ*, 553, 254
- Price, D. J., & Bate, M. R. 2007, *MNRAS*, 377, 77
- . 2008, *MNRAS*, 385, 1820
- Rao, R., Girart, J. M., Marrone, D. P., Lai, S.-P., & Schnee, S. 2009, *ApJ*, 707, 921
- Schneps, M. H., Lane, A. P., Downes, D., Moran, J. M., Genzel, R., & Reid, M. J. 1981, *ApJ*, 249, 124
- Sollins, P. K., Zhang, Q., & Ho, P. T. P. 2004, *ApJ*, 606, 943
- Surcis, G., Vlemmings, W. H. T., van Langevelde, H. J., & Hutawarakorn Kramer, B. 2012, *A&A*, 541, A47
- Tang, Y.-W., Ho, P. T. P., Girart, J. M., Rao, R., Koch, P., & Lai, S.-P. 2009a, *ApJ*, 695, 1399
- Tang, Y.-W., Ho, P. T. P., Koch, P. M., Girart, J. M., Lai, S.-P., & Rao, R. 2009b, *ApJ*, 700, 251
- Tang, Y.-W., Ho, P. T. P., Koch, P. M., & Rao, R. 2010, *ApJ*, 717, 1262
- Vaillancourt, J. E., et al. 2008, *ApJ*, 679, L25
- Vázquez-Semadeni, E., Kim, J., & Ballesteros-Paredes, J. 2005, *ApJ*, 630, L49
- Vlemmings, W. H. T., Diamond, P. J., van Langevelde, H. J., & Torrelles, J. M. 2006, *A&A*, 448, 597
- Wilson, T. L., Gaume, R., & Johnston, K. J. 1991, *A&A*, 251, L7
- Xu, Y., Reid, M. J., Menten, K. M., Brunthaler, A., Zheng, X. W., & Moscadelli, L. 2009, *ApJ*, 693, 413
- Zapata, L. A., Ho, P. T. P., Schilke, P., Rodríguez, L. F., Menten, K., Palau, A., & Garrod, R. T. 2009, *ApJ*, 698, 1422
- Zapata, L. A., Palau, A., Ho, P. T. P., Schilke, P., Garrod, R. T., Rodríguez, L. F., & Menten, K. 2008, *A&A*, 479, L25
- Zhang, Q., & Ho, P. T. P. 1995, *ApJ*, 450, L63+
- . 1997, *ApJ*, 488, 241
- Zhang, Q., Ho, P. T. P., & Ohashi, N. 1998, *ApJ*, 494, 636